Quantifying Bias and Precision of Kinetic Parameter Estimation on the PennPET Explorer, a Long Axial Field-of-View Scanner

Varsha Viswanath, *Member, IEEE*, Austin R. Pantel, Margaret E. Daube-Witherspoon, *Senior Member, IEEE*, Robert Doot, *Member, IEEE,* Mark Muzi, David A. Mankoff, and Joel S. Karp, *Life Fellow, IEEE*

***Abstract*—Long axial field-of-view (AFOV) PET scanners allow for full-body dynamic imaging in a single bed-position at very high sensitivity. However, the benefits for kinetic parameter estimation have yet to be studied. This work uses 1) a dynamic Geant4 Application for Tomographic Emission (GATE) simulation of [^{18}F]-fluorothymidine (FLT) in a modified NEMA IQ phantom and 2) a lesion embedding study of spheres in a dynamic [^{18}F]-fluorodeoxyglucose (FDG) human subject imaged on the PennPET Explorer. Both studies were designed using published kinetic data of lung and liver cancers and modeled using two tissue compartments. Data were reconstructed at various emulated doses. Sphere time-activity curves (TACs) were measured on resulting dynamic images, and TACs were fit using a two-tissue-compartment model ($k_4 \neq 0$) for the FLT study and both a two-tissue-compartment model ($k_4 = 0$) and Patlak graphical analysis for the FDG study to estimate flux (K_i) and delivery (K_1) parameters. Quantification of flux and K_1 shows lower bias and better precision for both radiotracers on the long AFOV scanner, especially at low doses. Dynamic imaging on a long AFOV system can be achieved for a greater range of injected doses, as low as 0.5-2 mCi depending on the sphere size and flux, compared to a standard AFOV scanner, while maintaining good kinetic parameter estimation.**

***Index Terms*—Dynamic imaging, fluorodeoxyglucose (FDG), fluorothymidine (FLT), Geant4 Application for Tomographic Emission (GATE) simulations, lesion embedding, long axial field of view PET, PennPET explorer.**

I. Introduction

DYNAMIC PET imaging offers biologic information beyond what is available from static images. When analyzed within the context of a two-tissue-compartment model, parameters of biologic relevance can be quantified, such as the flux constant through a key enzymatic step (K_i) for tracers with trapping, blood-to-tissue delivery (K_1) for tracers with or without trapping, tissue distribution volume (V_D) for fully reversible tracers, or specific receptor binding potential (BP) for tracers that reversibly bind to biological substrates such as receptors [1]. However, several factors can impact the resultant accuracy of parameters. Such factors include count statistics, lesion size relative to system spatial resolution, target uptake relative to background, and patient motion, including respiratory and gross motion. Uncertainties in estimating the measured blood input function can lead to errors in estimating kinetic parameters from dynamic images. Inadequate temporal sampling or radiotracer metabolite corrections, image noise, or partial volume errors when using small vessels may all contribute to inaccuracies in the blood input function [2]–[4].

Improving the quantitative accuracy of the underlying dynamic image data should enable more reliable kinetic parameter estimates. To increase the count statistics and improve quantitative accuracy, scanner sensitivity can be increased by extending the axial field-of-view (AFOV) of the scanner to capture a larger fraction of the coincident gammas or lines of responses (LORs) [5], [6]. This also enables dynamic studies in a single bed position covering the majority of the organs of interest. In this study, we investigated how improved count statistics from imaging on a long AFOV system affect kinetic parameter estimation using two tracers that were fit to either a reversible ($k_4 \neq 0$) or irreversible ($k_4 = 0$) two-tissue-compartment model.

Dynamic imaging is typically performed on standard AFOV PET scanners (< 30 cm long), usually over a single bed position. Although methods have been developed to dynamically image the whole body by acquiring repeat whole body scans over multiple bed positions [7], [8], they do not allow continuous temporal sampling of distant organs with the very high sensitivity levels of long AFOV systems. Conversely, systems with AFOVs that have been extended by introducing axial gaps between detectors rather than more detector coverage will not have the very high sensitivity of long AFOV scanners, but will allow for continuous temporal sampling of distant organs [9]–[12]. This work studies the effect on kinetic parameter bias and precision of long AFOV scanners with high sensitivity. In recent years, the sensitivity of PET scanners has increased by extending the AFOV up to 26 cm, allowing

Manuscript received February 3, 2020; revised May 16, 2020 and July 13, 2020; accepted August 24, 2020. Date of publication September 2, 2020; date of current version November 3, 2020. This work was supported in part by NIH under Grant R33-CA-225310, Grant R01-CA113941, and Grant R50-CA211270. *(Corresponding author: Varsha Viswanath.)*

Varsha Viswanath is with the Bioengineering Department, University of Pennsylvania, Philadelphia, PA 19104 USA (e-mail: vvisw@seas.upenn.edu).

Austin R. Pantel, Margaret E. Daube-Witherspoon, Robert Doot, David A. Mankoff, and Joel S. Karp are with the Department of Radiology, University of Pennsylvania, Philadelphia, PA 19104 USA.

Mark Muzi is with the Department of Radiology, University of Washington, Seattle, WA 98195 USA.

Color versions of one or more of the figures in this article are available online at http://ieeexplore.ieee.org.

Digital Object Identifier 10.1109/TRPMS.2020.3021315

for better quality dynamic images, and more axial coverage. Scanners with significantly longer AFOV have been introduced in the last year to further increase the sensitivity and the axial coverage [13]–[18]. There are currently three such long AFOV scanners currently in use: two 195-cm long uExplorer scanners from United Imaging at UC Davis and Zhongshan Hospital and the 70-cm long PennPET Explorer at UPenn [19], [20]. The total sensitivity of these scanners increases by a factor of $20\times - 40\times$ compared to a standard AFOV scanner due to the longer axial extent of the detectors and the increased axial acceptance angle. However, the sensitivity at a single axial position (i.e., point source sensitivity) in an attenuating medium such as a patient only improves by $2 \times -3\times$ as a result of attenuation of oblique LORs [18]. Because this gain in sensitivity is mostly realized by an AFOV of 70-cm [18], [21], gains based on sensitivity for dynamic imaging on a long AFOV scanner can be tested on a scanner with an axial length of 70 cm and applied to longer devices.

Simulations predicted that the increased sensitivity of long AFOV systems result in an improvement in lesion detectability [22], [23] which has been substantiated by measurements on the PennPET Explorer [24]. Measured human subject data on the PennPET Explorer has also demonstrated that the increased sensitivity of the scanner enables imaging at up to 24 h after injection of fluorodeoxyglucose (FDG) [25]. Thus far, a direct Patlak parametric image reconstruction method has been designed and applied to dynamic FDG human subject data. Results showed improved parametric image noise compared to indirect estimation methods [26]. Additionally, Wang *et al.* [27] have implemented a time-varying model to estimate delivery (K_1) of FDG to tissues such as the kidney. UC Davis has also shown dynamic images with good image quality (IQ) for time frames as short as 1 s for the whole body and 100 ms for the heart [28]. While the images from these systems are qualitatively striking, the impact of the increased sensitivity of long AFOV systems in comparison to standard AFOV scanners on quantitative accuracy, including kinetic parameter estimation, has not been studied. This work focuses on studying how the increased sensitivity affects kinetic parameter estimation as a function of injected radioactive dose.

The PennPET Explorer has been built and tested as a three ring-segment (70-cm AFOV) scanner, where each ring has a 23-cm AFOV. Static and dynamic studies have been performed on both clinical (e.g., [^{18}F]-FDG or [^{68}Ga]-DOTATATE) and research tracers to test its operation and demonstrate its capabilities [25]. We have generated high quality images from dynamic studies and low-noise time-activity curves (TACs) with time frames as short as 1 s.

Herein, we present a series of studies using both simulated and measured data from the early PennPET Explorer prototype to understand how imaging on long AFOV systems impacts kinetic parameter estimation of dynamic studies. We compare kinetic parameter estimates from a 70-cm long AFOV system to a single-ring system, meant to represent a standard AFOV scanner. We examine the accuracy and precision of kinetic parameter estimation for dynamic imaging as a function of count statistics (i.e., injected dose), lesion size, and modeling methodology for two tracers, [^{18}F]-fluorothymidine (FLT) and [^{18}F]-FDG, which are typically modeled using two-tissue-compartment models, with a focus on estimation of flux (K_i) and delivery (K_1). Ultimately, we aim to optimize the approach for dynamic imaging in patient studies on long AFOV PET systems.

II. Methods

We performed two studies to primarily assess the relationship between improved count statistics and kinetic parameter estimation. The first was a simulation study of the modified NEMA IQ phantom designed to emulate dynamic imaging of [^{18}F]-FLT. The second was an emulation study where measured lesions are dynamically embedded into a dataset of a normal human subject injected with [^{18}F]-FDG and dynamically imaged on the PennPET Explorer. Both tracers can be modeled using two-tissue-compartments. FLT was selected to represent a generic two-tissue-compartment dynamic tracer where $k_4 \neq 0$ (reversible), and FDG was selected to study a well characterized dynamic tracer where $k_4 = 0$ (irreversible) for most organs. Both tracers had sufficient literature reports on dynamic imaging with estimated kinetic parameters to design these studies [29]–[34], and raw measured dynamic patient data were readily available to guide study design.

A. Dynamic FLT Phantom Monte Carlo Simulation

1) Scanner Geometry and GATE Simulations: All simulations were done using Geant4 Application for Tomographic Emission (GATE) v8.0 [35]. We extended a GATE model of the Philips Vereos scanner from an AFOV of 16.4 cm to 23 cm to form a single ring-segment representative of a scanner with the axial length of standard commercial PET systems. Three of these ring-segments were abutted to form the simulation of the 70-cm AFOV PennPET Explorer (Fig. 1). Both the 23-cm ring-segment and the 70-cm PennPET Explorer were composed of $3.86 \times 3.86 \times 19$-mm^3 LYSO crystals resulting in a 4.0-mm spatial resolution, and all simulations were run with a timing resolution of 320 ps to match the Philips Vereos timing resolution when operated at room temperature [19]. GATE simulations included modeling of positron range, acollinearity, and radioactive decay, as well as trues, randoms, and both Compton and Rayleigh scattering. Light sharing between crystals and LOR efficiency were modeled when converting GATE files into list-mode files to properly emulate the electronics of the Vereos based on benchtop measurements of the detector elements. Prior work by Trindade *et al.* [36] implemented these models in GATE and showed good correspondence between performance of the Vereos simulations and measurement. Normalization correction for all simulations was estimated using a 60-cm diameter cylinder filled with ^{18}F and the ratio of measured data to ideal data was used to create the correction factors [37].

2) Generation and Reconstruction of Dynamic FLT Phantom Data: To generate the ideal TACs for dynamic simulations, rate constants from prior studies of the PET proliferation tracer [^{18}F]-FLT were utilized [29]. FLT is an analog of thymidine, a building block for DNA. Measures of FLT flux

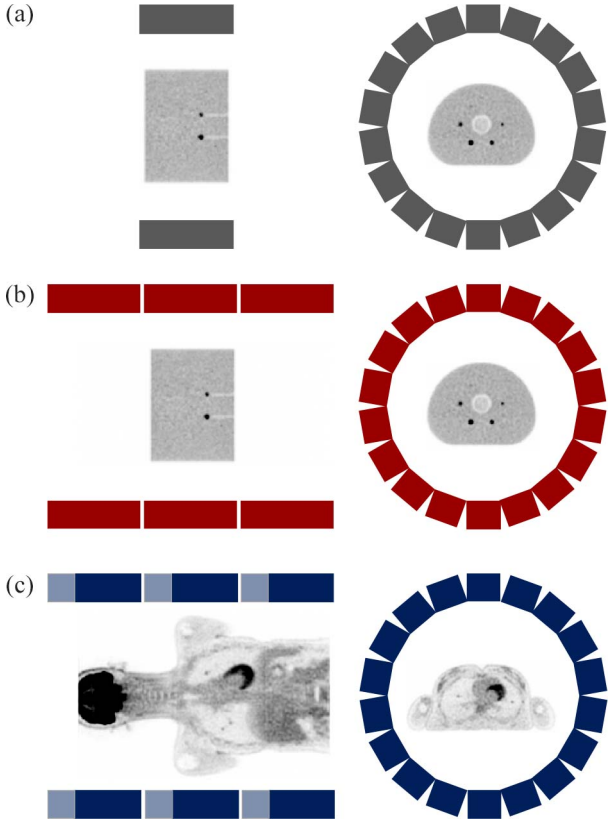

Fig. 1. Scanner geometries depicted for the (a) 23-cm simulated ring-segment and FLT phantom, (b) 70-cm simulated PennPET Explorer and FLT phantom, and (c) measured PennPET Explorer and normal subject scanned with FDG (c). Light blue sections on the PennPET Explorer reflect data inactive regions. The modified IQ phantom is depicted on the simulated 23-cm and 70-cm scanners while the human subject with dynamic lesions embedded is depicted on the PennPET Explorer.

TABLE I
KINETIC PARAMETERS FOR THE DYNAMIC FLT SIMULATION

	Low	Medium	High	Bkgd (muscle)
v_B	0.05	0.05	0.05	0.05
K_1	0.074	0.135	0.2	0.0235
K_1/k_2	0.35	0.68	1.3	0.58
k_3	0.21	0.175	0.15	0.03
k_4	0.04575	0.02015	0.01525	0.019
Flux	**0.0369**	**0.0632**	**0.0987**	**0.01**

through thymidine kinase, a rate-limiting enzyme for thymidine incorporation into DNA, have been shown to correlate with measures of tumor proliferation, including Ki-67 values, a marker of cellular proliferation determined from tumor biopsy material [38]. As such, FLT flux provides a measure of tumor growth that can be used to assess response to therapy. The dynamic behavior of different organs in the FLT simulations was based on published dynamic FLT data from lung cancer patients. Kinetic parameters were selected to emulate low, medium, and high flux lung tumors based on these published series [29], [30]. Kinetic parameters for the background were based on muscle tissue from the same lung cancer patient studies [29], [30]. The blood input function was based on the left ventricular (LV) blood pool measured in dynamic FLT

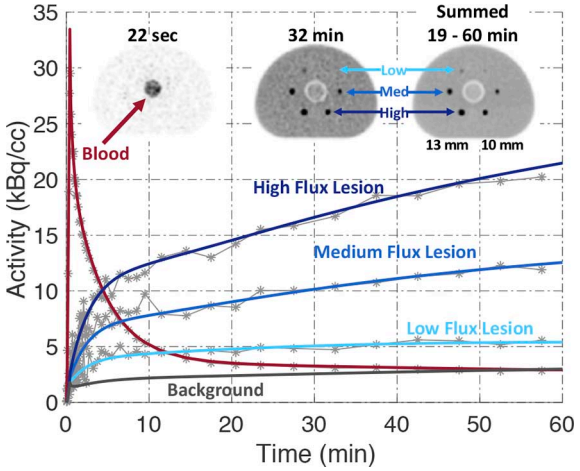

Fig. 2. Ideal simulated FLT TACs for the low, medium, and high uptake lesions (blue) in the modified NEMA IQ phantom along with the blood input function (red). Images (2-mm slice) of the modified IQ phantom for the full-dose dataset are shown at the top. An early frame clearly (at 22 s, 5-s duration) shows blood pool uptake and a later frame (at 32 min, 5 min duration) shows uptake in the low (top), medium (middle), and high (bottom) flux lesions and the difference between the 13 mm (left) and 10 mm (right) lesions. Example data points from a single dynamic phantom simulation, are shown in gray for the 10-mm spheres at full dose (4 mCi, 148 MBq).

images from a breast cancer patient after a 4 mCi (148 MBq) injection of FLT, fit to a tri-exponential model. For this study, we ignored the metabolites in the blood. This blood input function, along with the selected kinetic parameters, was used to generate representative ideal TACs for low, medium, and high flux tumors using a two-tissue-compartmental model and the Stella Architect software package (isee Systems Inc., Lebanon, NH, USA). Because the measured fit blood curve was assumed to be the true FLT plasma input function that was used to generate the tissue curves as inputs to the simulation, any metabolites in this curve will not affect results of the study. The selected kinetic parameters are shown in Table I.

The simulated dynamic FLT phantom was modified from a NEMA IQ phantom with an axial extent of 21 cm [39]. The six spheres in the phantom were modified to represent small lung lesions: three with a 10 mm diameter and three with a 13 mm diameter. Each of the three spheres was simulated with uptake profiles to emulate the dynamic behavior of low, medium, and high flux lesions following their ideal TACs (Fig. 2). The lung insert in the center of the phantom was altered to have the attenuation of water and was dynamically simulated to emulate the blood TAC while the background region was dynamically simulated to emulate the muscle or background TAC. For purposes of the simulation, these curves were discretized into 500-ms segments. The phantom was placed in the center of the AFOV for the simulations. The phantom was simulated for 60 min on both the 23-cm ring segment and the 70-cm PennPET Explorer simulation [Fig. 1(a) and (b)] and coincidence data written into list-mode files.

The list-mode data were parsed into 45 frames (16×5 s, 7×10 s, 5×30 s, 5×60 s, 5×180 s, 7×300 s) [30]. Each frame was then subsampled from a full dose of 4.0 mCi

(148 MBq) into one-half, one-quarter, one-eighth, and one-sixteenth the dose, roughly corresponding to emulated doses of 2.0, 1.0, 0.5, and 0.25 mCi (74, 37, 18.5, and 9.25 MBq, respectively. Each of these five datasets was then bootstrapped using list-mode bootstrapping with replacement to generate 20 statistical replicates per dataset [40]. The list-mode data were reconstructed using a blob-based time-of-flight list-mode ordered subsets expectation maximization (TOF-LM-OSEM) algorithm (4 iterations and 25 subsets) and binned into 2-mm^3 isotropic voxels [41]. All corrections, including scatter, randoms, attenuation, and normalization corrections were applied. Scatter correction was estimated using 3-D time-of-flight single-scatter-simulation [42], while randoms correction was estimated using a delayed timing window.

3) Data Analysis for Simulated Dynamic FLT Phantom Images: Spherical volumes of interest (VOIs, diameter equal to the physical sphere diameter) were centered over all spheres and circular regions of interests (ROIs) were drawn over several slices of the lung insert and the mean value of each region was corrected for scan duration, decay, and partial volume effects. A separately simulated uniform cylinder was used to determine the scanner calibration factor to convert image counts into activity concentration units (Bq/cc).

Partial volume correction (PVC) was applied so that measured TACs would agree with the true TAC and minimize systematic bias in kinetic parameter estimation. This PVC method was designed to minimize adding noise to the TACs. PVC was based on the known ideal contrast for each frame and the measured contrast recovery coefficient (CRC) value for a given sphere size. Partial volume effects are defined as the ratio of the measured contrast (H/B) over the actual contrast (a). We calculated H/B using the known contrast and rearranging the CRC equation so that $H/B = CRC * (a-1) + 1$. The multiplicative PVC was then defined as $a/(CRC*(a-1)+1)$. CRC for a given sphere size was measured on a uniform cylinder dataset with embedded spheres reconstructed using the TOF-LM-OSEM algorithm.

The generated TAC data were fit using PMOD v3.7 (PMOD Technologies LLC, Zürich, Switzerland). The same two-tissue-compartment model used for data simulation was applied to the resulting simulated image data with model estimation starting values of 0.05 mL/g, 0.2 mL/g/min, 2.0 mL/g, 0.2 min^{-1}, and 0.02 min^{-1} for v_B, K_1, K_1/k_2, k_3, and k_4, respectively, based on prior work with thymidine tracers [30], [43]; all parameters were fit in the model. Calculated weighting was applied to the model using Poisson weighting derived from the measured value, frame duration, and decay based on the frame mid-time.

For each of the six spheres and five emulated doses, the mean ($\bar{x}$) and standard deviation ($\bar{s}$) of both flux (K_{FLT}) and delivery (K_1) were calculated across the 20 bootstrapped replicates. Bias was calculated as $100\% * (\bar{x} - \mu)/\mu$ and percent standard deviation (% SD) was calculated as $100\% * \bar{s}/\mu$, where μ is the known value of the kinetic parameter or flux for the corresponding simulated dataset. We use the % SD as a measure of precision.

B. Dynamic FDG Lesion Embedding Study

Spheres measured in air were embedded into each frame of a dynamic dataset from a human FDG subject acquired on the PennPET Explorer to emulate a human study with lesions.

1) Scanner Geometry: All data were taken on the PennPET Explorer, a 70-cm long AFOV PET scanner built using the Philips digital photon counting tiles, which consist of an array of 3.86 × 3.86 × 19 mm^3 LYSO crystals coupled to a digital SiPM array. The scanner is composed of three 23-cm AFOV rings, of which 6.6-cm is currently inactive due to data readout limitations [Fig. 1(c)], unlike the simulated scanner that did not have inactive regions. The inactive regions result in half the total sensitivity and introduce small axial image noise variations. Once these regions are active, the scanner will match the simulated 70-cm scanner. The PennPET Explorer has a measured spatial resolution of 4.0 mm, energy resolution of 12%, sensitivity of 54 kcps/MBq, and a timing resolution of 250 ps. The timing resolution is improved compared to the Philips Vereos by cooling the system to 5 °C, thus reducing the dark noise, and using a lower timing trigger level [19].

2) Human Subject Data Acquisition: Dynamic lesion embedding was performed for FDG, a tracer of glucose metabolism and the most widely used PET imaging agent in clinical practice, especially for cancer patients. Dynamic FDG imaging has been shown to improve the ability to measure cancer response to treatment, especially for low uptake tumors [44]. To obtain the background dynamic tissue biodistribution data for this study, a normal human subject was injected with 500 MBq of FDG and imaged dynamically for 60 min on the PennPET Explorer. The subject was positioned such that the top of her head aligned with the edge of the scanner and the head, torso, and abdomen were within a single bed position. List-mode data were parsed into 70 frames (20×1 s, 10×2.5 s, 7×5 s, 7×10 s, 9×30 s, 5×1 m, 6×3 m, 6×5 m) to accurately capture the bolus injected into the patient (i.e., a quick 2-s injection). For attenuation correction, CT data were acquired on a clinical PET/CT system and registered to the PET dataset using rigid body registration [25].

3) Sphere-in-Air Data Acquisition: Sphere-in-air data were also acquired on the PennPET Explorer for dynamic embedding into the subject's dataset. A 6-mm and a 10-mm sphere were filled with 37–74 MBq of FDG and imaged in air over a 3-D grid of positions to cover possible locations where a lesion may occur within a human subject. Sufficient sphere data were acquired in list-mode at each location such that the desired number of list-mode events could be filtered and embedded in the data to represent a lesion with given uptake based on a previously established methodology [45]. A sphere size smaller than 10-mm was chosen to further test the improved spatial resolution and sensitivity of the scanner. Twenty-six sphere locations (10 liver, 8 right lung, and 8 left lung) were selected to embed dynamically into the human subject dataset, as described below. The spheres in this lesion embedding study were placed over a large axial range in the scanner where axial sensitivity is not constant. Spheres for the previously described GATE simulation were placed

TABLE II
KINETIC PARAMETERS FOR THE DYNAMIC FDG MEASUREMENT

	Lung			Liver		
	Low Flux	Medium Flux	High Flux	Low Flux	Medium Flux	High Flux
v_B	0.170	0.170	0.170	0.200	0.170	0.120
K_1	0.100	0.178	0.133	0.119	0.194	0.086
k_2	0.219	0.550	0.044	0.487	0.782	0.031
k_3	0.074	0.250	0.070	0.113	0.279	0.404
k_4	0	0	0	0	0	0
K_i	***0.0253***	***0.0556***	***0.0817***	***0.0224***	***0.0510***	***0.0799***

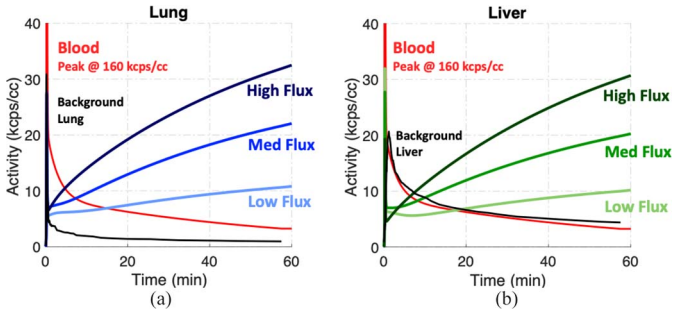

Fig. 3. Ideal TACs for FDG lesion embedding for the (a) lung and (b) liver.

near the center of the AFOV, which ensured maximum sensitivity benefits of the 70-cm scanner compared to the 23-cm scanner.

4) Generation and Reconstruction of Dynamic FDG Data With Embedded Lesions: Generation of ideal dynamic FDG lesion TACs was based on a two-tissue-compartment/3-parameter model of FDG kinetics. As in the FLT simulations, published literature kinetic values for dynamic FDG lung and liver cancer studies were used to select a set of kinetic parameters to represent low, medium, and high uptake lesions. Kinetic parameters selected for lung lesions were derived from published patient data with a variety of lung cancers, and parameters for liver lesions were acquired from FDG PET data of patients with metastatic liver cancer of colorectal origin (see Table II) [31]–[34]. Ideal low, medium, and high flux TACs in the lung and liver were generated using the human subject's LV blood curve fit to a tri-exponential model, and a two-tissue-compartment model with trapping ($k_4 = 0$) was assumed for all lesions using STELLA (Fig. 3). FDG kinetic parameters were independently selected to fall within the biologic range of dynamic FDG data, but variations will not impact the study, since they were used to generate the lesion TACs and set as ground truth.

Lesions were embedded independently in each of the 70 frames using a modified lesion embedding methodology. Based on previously published work, the number of list-mode events for each sphere was calculated using the desired contrast and local background uptake at that time point [45]. List-mode events from the different spheres were merged together on a frame-by-frame basis and then statistically attenuated using the probability of attenuation through each LOR of the human subject from the human subject's attenuation image.

Prior work with list-mode-based lesion-embedding methodology only embedded positive lesions (i.e., lesions with higher uptake than background) and the attenuated sphere-in-air events were merged with the background events prior to reconstruction [45]. The early portion of the lesion TACs, which are driven by delivery of tracer to the lesion, were not designed to use the dual blood supply of the liver as the blood input function, but rather an arterial input function as would be typical of a liver metastasis. This resulted in lower lesion uptake during the early time points of the ideal lesion TACs compared to the measured liver background. Therefore, events needed to be removed from the embedded lesion location. Because list-mode event data can only be added, not removed, we instead implemented lesion embedding in histo-image format, a binned representation of the data [46]. Both sphere-in-air and human subject list data were binned into 4-mm histo-images (144 × 144 × 160 slices × 40 views × 9 tilts), where the sphere-in-air list-mode data were first statistically attenuated. Histo-images from both the human subject and the lesions were then added or subtracted for each frame to create a histo-image with embedded lesions for each frame. Each frame was then reconstructed using direct image reconstruction for time-of-flight PET (DIRECT) [46], an iterative time-of-flight reconstruction algorithm based on the histo-image data format (50 iterations; row-action maximum likelihood—RAMLA—update [47]), into 4 mm^3 voxels. The reconstruction used 2.0-mm line-of-response modeling and image filtering to match the image noise of the blob-based TOF-LM-OSEM reconstruction used for the simulated data. Scatter, attenuation, normalization, and randoms corrections were applied [48]. Images were then resampled in the spectral domain to create 2 mm^3 images to allow more accurate definition and placement of the evaluated VOIs. We have observed that resampling decreases the measured sphere CRC by only 1%–2% compared with reconstructing directly into 2-mm^3 voxels but with reduced reconstruction time.

This method of lesion embedding was applied to generate six datasets at a 13.5 mCi (500 MBq) FDG dose that included two sphere sizes, 6-mm and 10-mm lesions, and three fluxes. The six list-mode datasets of the combined lesion and background FDG data were also subsampled to emulate FDG doses of 9.0, 4.5, 2.25, 0.9, and 0.45 mCi (333, 167, 83.3, 33, and 16.7 MBq, respectively), similar to the approach used for the FLT phantom simulations, to create 30 more datasets that were

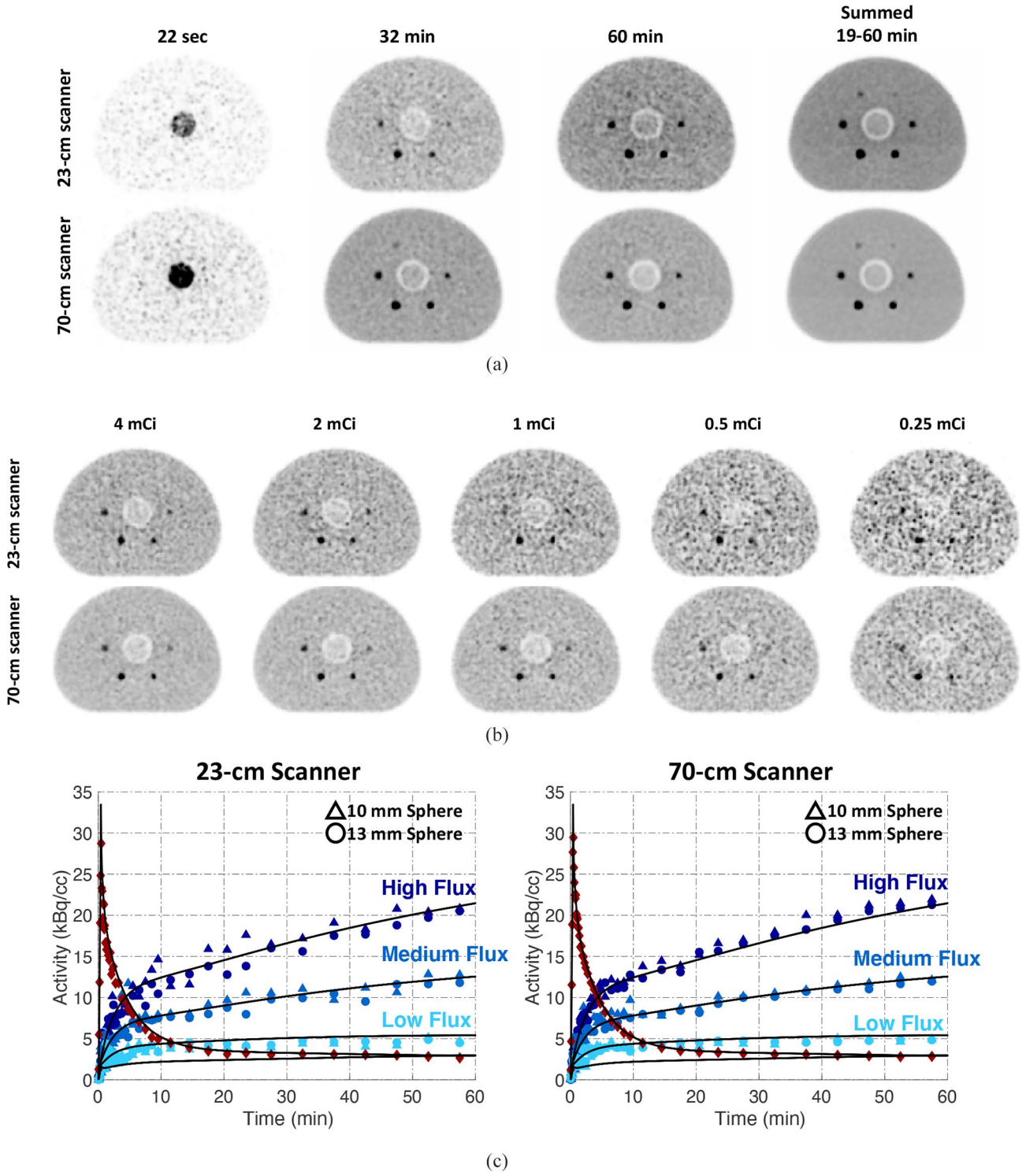

Fig. 4. (a) Representative images of the modified IQ phantom at full-dose on both the 23-cm (top) and 70-cm scanners (bottom) at various time points: 22 s (5-s duration), 32 min (5 min), 60 min (5 min), and summed 19–60 min (left to right). (b) Axial 2-mm slices of the final frame (5 min duration) shown for 4-0.25 mCi (left to right) and for the 23-cm (top) and 70-cm (bottom) scanners. (c) TACs with measured data at full-dose for all sphere sizes and fluxes for both the 23-cm scanner (left) and the 70-cm scanner (right).

similarly deposited into histo-images and reconstructed using DIRECT.

5) Data Analysis for Dynamic FDG Data With Embedded Lesions: From their known locations, VOIs were drawn over each sphere, corrected for scan duration, decay, and partial volume effects. TACs were created using the VOI mean. PVC was implemented using the known contrast at each time point and sphere size, as described for the simulation analysis. The 10 liver spheres and 16 lung spheres were used as replicates. Blood input data was measured from the left ventricle and fit to a tri-exponential for each dataset.

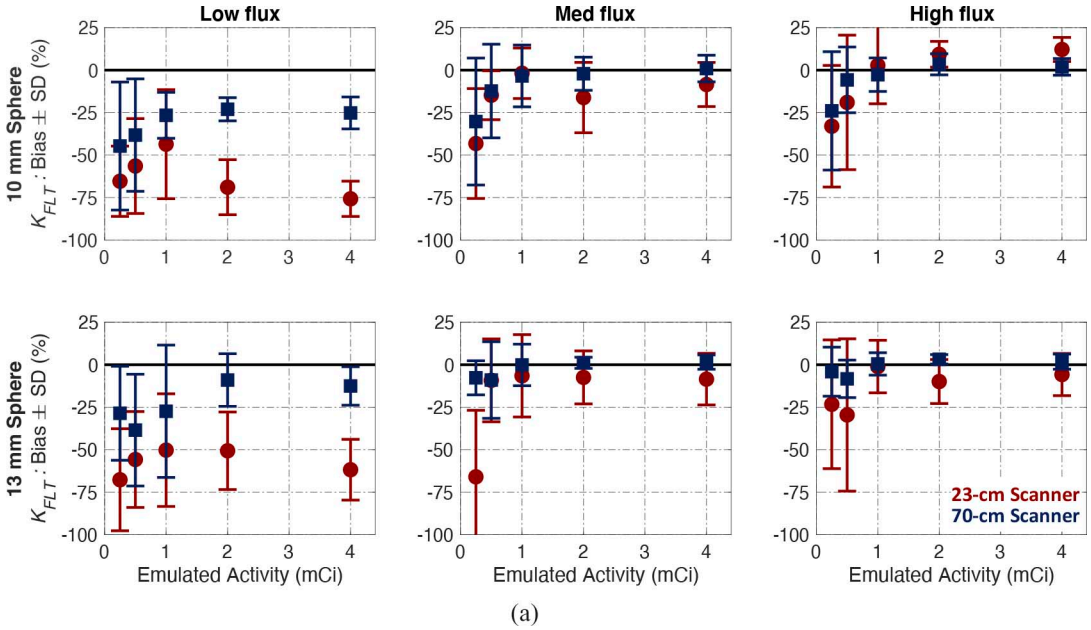

Fig. 5. (a) Bias and (b) % SD results quantifying flux (K_{FLT}) fit using a two-tissue-compartment model. Data are from the FLT simulation for the 23-cm ring-segment (red) and the 70-cm PennPET Explorer simulation (blue). Results are shown for the low, medium, and high (left to right) flux spheres and for the 10 mm (top) and 13 mm (bottom) spheres.

Data were fit in PMOD using both the Patlak graphical method [49] and the two-tissue-compartment FDG model with v_B and k_4 fixed at 0.15 and 0, respectively, where 0.15 falls within the range of the ideal v_B values, and a k_4 of 0 was used to generate the ideal TACs. Parameter estimation starting values for K_1, k_2, and k_3 were 0.102 mL/ccm/min, 0.13 1/min, 0.062 1/min, respectively; no weighting was applied during fitting. For each dataset the mean and standard deviation for the 10 liver spheres and 16 lung spheres were determined to estimate the bias and % SD of the kinetic parameters, as previously described.

III. Results

A. Dynamic FLT Phantom Monte Carlo Simulation

Representative images of the modified IQ phantom are shown in Fig. 4 at full-dose for both the 23-cm and 70-cm scanners, along with corresponding images of the final frame for all emulated doses studied. Early time point images at 22 s highlight the blood peak in the central rod of the phantom. Later images at 32 and 60 min highlight the six spheres representing embedded lesions. At 32 min, the low flux spheres are not visible on the 23-cm scanner, and the 10-mm medium flux sphere is only barely visible. On the 70-cm scanner, both

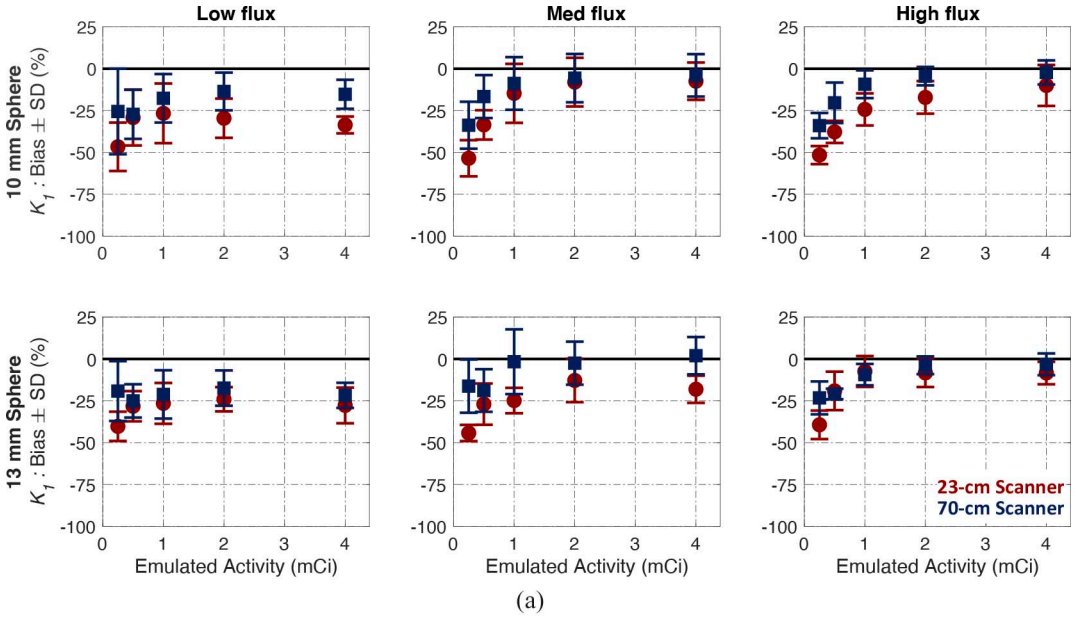

(a)

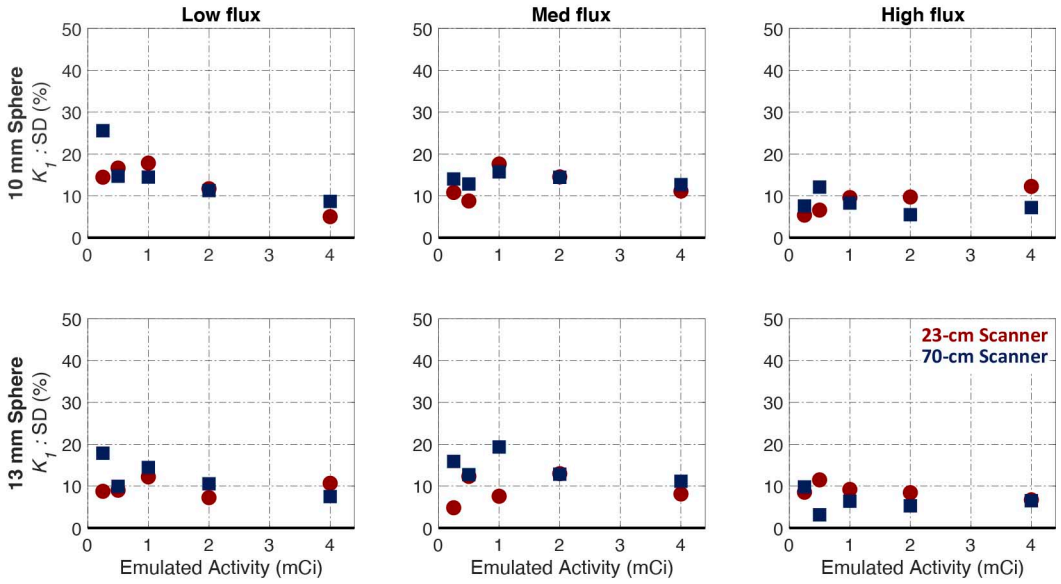

(b)

Fig. 6. (a) Bias and (b) % SD results quantifying delivery (K_1) fit using a two-tissue-compartment model. Data were measured from the FLT simulation for both the 23-cm ring-segment (red) and the 70-cm PennPET Explorer simulation (blue). Results are shown for the low, medium, and high (left to right) flux spheres and for the 10 mm (top) and 13 mm (bottom) spheres.

the 13-mm low flux and both 10-mm medium flux spheres are clearly visible at 32 min. At 60 min, the 10-mm low flux sphere cannot be visualized on either scanner. The summed images show the location of the low flux 10-mm sphere. Measured TACs from the 23-cm and 70-cm geometries agree well with ideal input TACs [Fig. 4(c)].

The bias and % SD of FLT flux (K_{FLT}) fit using a two-tissue-compartment model are shown in Fig. 5 for the six spheres on the 23-cm and 70-cm geometries at doses ranging from 4 mCi (148 MBq) to 0.25 mCi (9.25 MBq). Overall, results from the IQ phantom study show that bias is close to zero for medium and high flux lesions at higher doses, but larger at lower doses. Bias is consistently large for the low flux lesions regardless of dose or lesion size, though the 70-cm scanner has less bias that the 23-cm scanner. Precision for the 70-cm scanner geometry is generally better (i.e., lower % SD) than that for the 23-cm scanner geometry, especially for the medium and high flux spheres.

The bias and % SD of the estimated FLT delivery parameter (K_1) fit using the two-tissue-compartment model is shown in Fig. 6. Overall, delivery (K_1) 1) has a bias close to zero for the medium and high flux spheres; 2) has a lower bias than that for flux for all spheres; and 3) has slightly lower bias for the 70-cm scanner geometry compared to that for the 23-cm scanner geometry. Precision measures show little difference between the 23-cm and 70-cm scanner lengths when estimating K_1, and

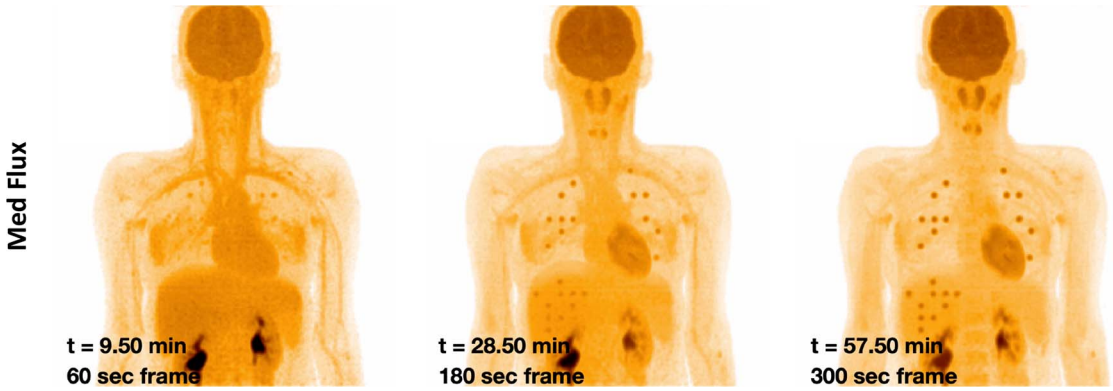

Fig. 7. Maximum intensity projection images showing early, middle, and late (left to right) frames for the medium flux lesion datasets. 10 lesions are visible in the liver, seven lesions are visible in the right lung, and six lesions are visible in the left lung.

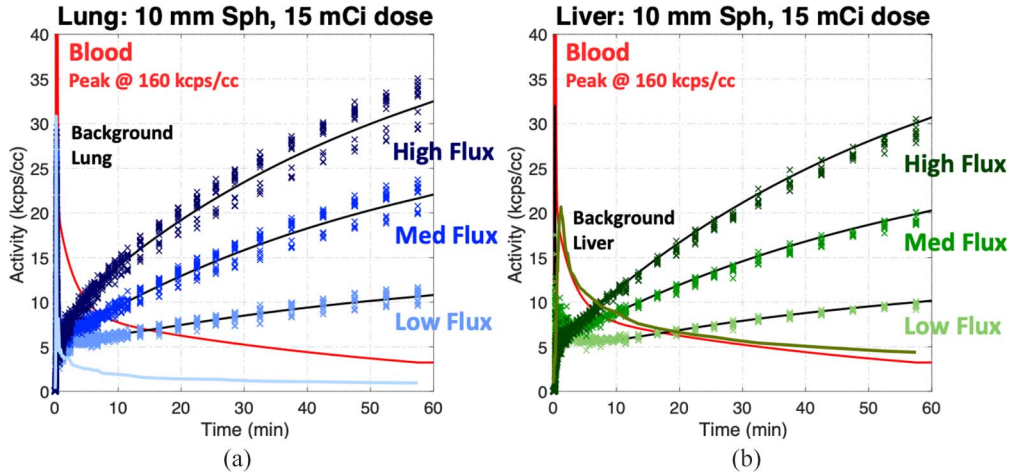

Fig. 8. Plots depicting the correspondence between measured sphere data (colored x's) and ideal curves (black lines) for embedded spheres in the (a) lung and (b) liver. Data shown are for the 10-mm spheres from the 15 mCi dose dataset. Also shown are the measured blood curve (red), background lung curve (sky blue), and background liver curve (olive green).

overall, % SD is 10% for high flux spheres and 20% or lower for medium and low flux spheres at all doses.

B. Dynamic FDG Lesion Embedding Study

Maximum intensity projection images of lesions embedded in the lung and liver of the human subject are shown for the medium flux spheres in Fig. 7 at three time points. Lesions were placed volumetrically through the image; 10 liver lesions and 13 lung lesions are visible. Measured TACs for these lesions (Fig. 8) at full dose (13.5 mCi and 500 MBq) reflect the accuracy of the lesion embedding methodology.

Bias and % SD results for flux (K_i) and delivery (K_1) are shown in Figs. 9–11. Results are shown for 6- and 10-mm spheres embedded in the liver and lung at low, medium, and high flux as a function of emulated activity. Because a subset of lesions was located within the PennPET Explorer's data readout inactive regions, single ring analyses could not be done. However, to compare results with a single ring scanner, one can compare PennPET Explorer results to values at one-third the emulated dose, since the axial sensitivity of a standard AFOV scanner is roughly one-third that of the PennPET Explorer [21].

Results quantifying bias and % SD of flux using Patlak graphical modeling are shown in Fig. 9. Results show bias is close to zero and stable until the lowest doses, while % SD for the 6-mm sphere is higher than that of the 10-mm sphere, as expected. Bias and precision both improve (i.e., lower bias and % SD) as the dose increases, showing similar trends across all spheres.

Fig. 10 shows the bias and % SD of FDG flux estimated using a two-tissue-compartmental model. Results show a systematic nonzero positive bias (20%–25% lung and 10%–15% liver) in the estimation of flux that is independent of dose. Precision measurements at low doses are better using a two-tissue-compartment model than those obtained using Patlak analysis and are largely independent of dose except for the lowest activities. The % SD decreases with higher flux and is greater for the 6-mm spheres compared to the 10-mm spheres, as expected, with both Patlak and two-tissue-compartmental fitting.

Fig. 11 shows the bias and % SD of the FDG delivery parameter (K_1) estimated using a two-tissue-compartmental fit. K_1 values show a systematic nonzero negative bias (25% lung and 25%–50% liver) for the low and medium flux spheres that increases at lower doses. The high flux lung and liver lesions

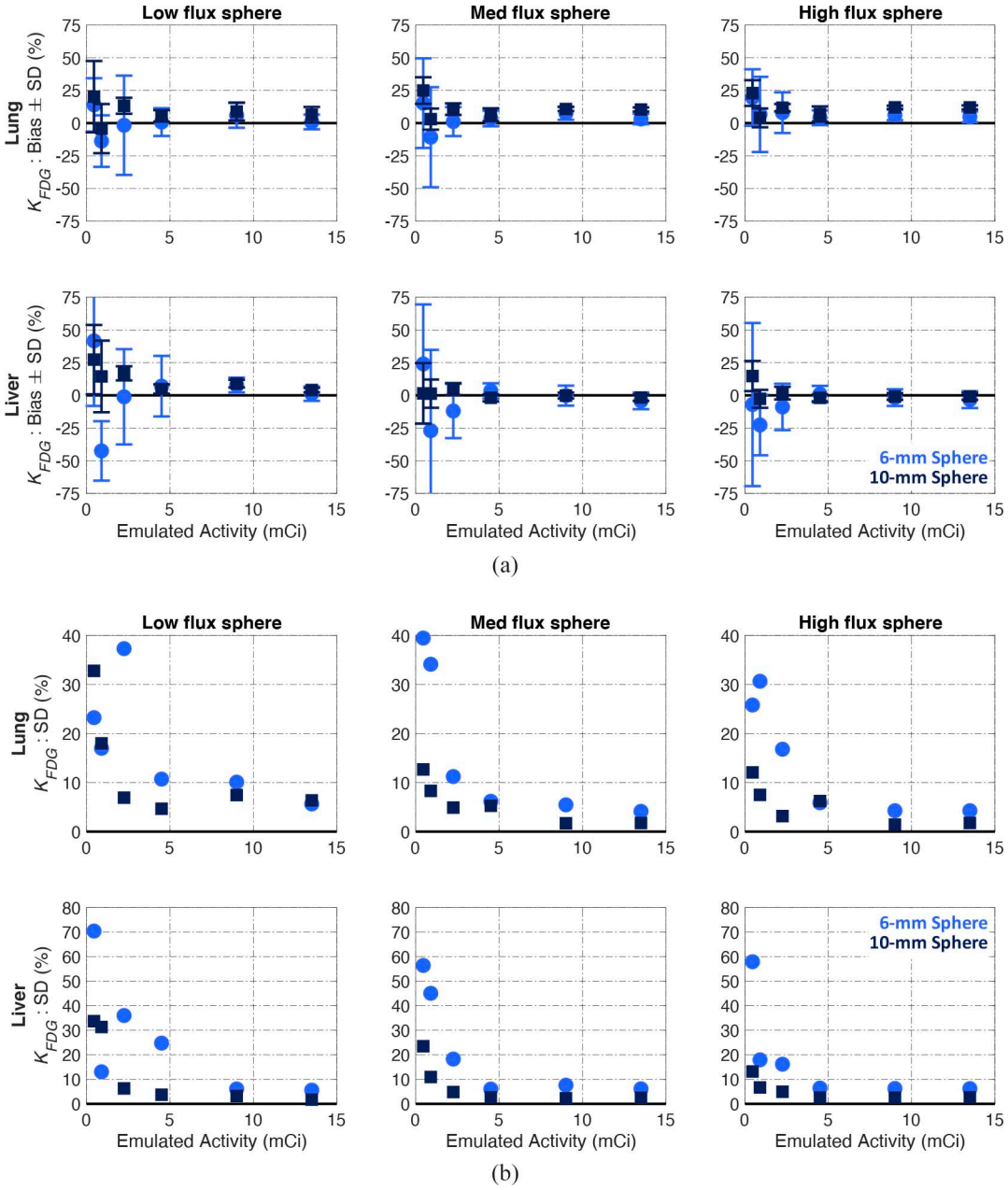

Fig. 9. Bias (a) and % SD (b) results quantifying flux (K_{FDG}) using Patlak graphical analysis as measured from the FDG PennPET Explorer emulation for the 6-mm sphere (medium blue) and the 10-mm sphere (dark blue). Results are shown for the low, medium, and high (left to right) flux spheres for the lung (top) and liver (bottom). Note the y-axis for the liver plots of % SD has a maximum of 80% as opposed to 40% for all other % SD plots.

show biases closer to zero for all emulated doses. The % SD of K_1 is low except for the 6-mm sphere in the lung, which had relatively high % SD at low and medium fluxes. The % SD does not show a systematic trend as a function of dose but does show a slight decrease for higher flux spheres.

IV. Discussion

Through a series of simulation studies, we have demonstrated improvements in accuracy of quantitative kinetic parameter estimation with a long AFOV scanner compared to a standard AFOV scanner. We studied two tracers: FLT which was modeled using a reversible two-tissue-compartment model and FDG which was modeled using an irreversible two-tissue-compartment model. The FLT study was implemented using monte-carlo simulations in GATE, while the FDG study utilized dynamic lesion embedding in dynamic FDG data measured on the PennPET Explorer. We then studied the performance of such a system in quantifying tracer kinetics using embedded lesions in a healthy patient with decreasing administered activities and smaller lesion size.

The dynamic FLT simulations (Figs. 5 and 6) demonstrate overall better kinetic parameter estimation—both improved bias and precision of delivery and flux estimates—with the 70-cm scanner geometry compared to the 23-cm simulated scanner. Improvements were particularly accentuated in low

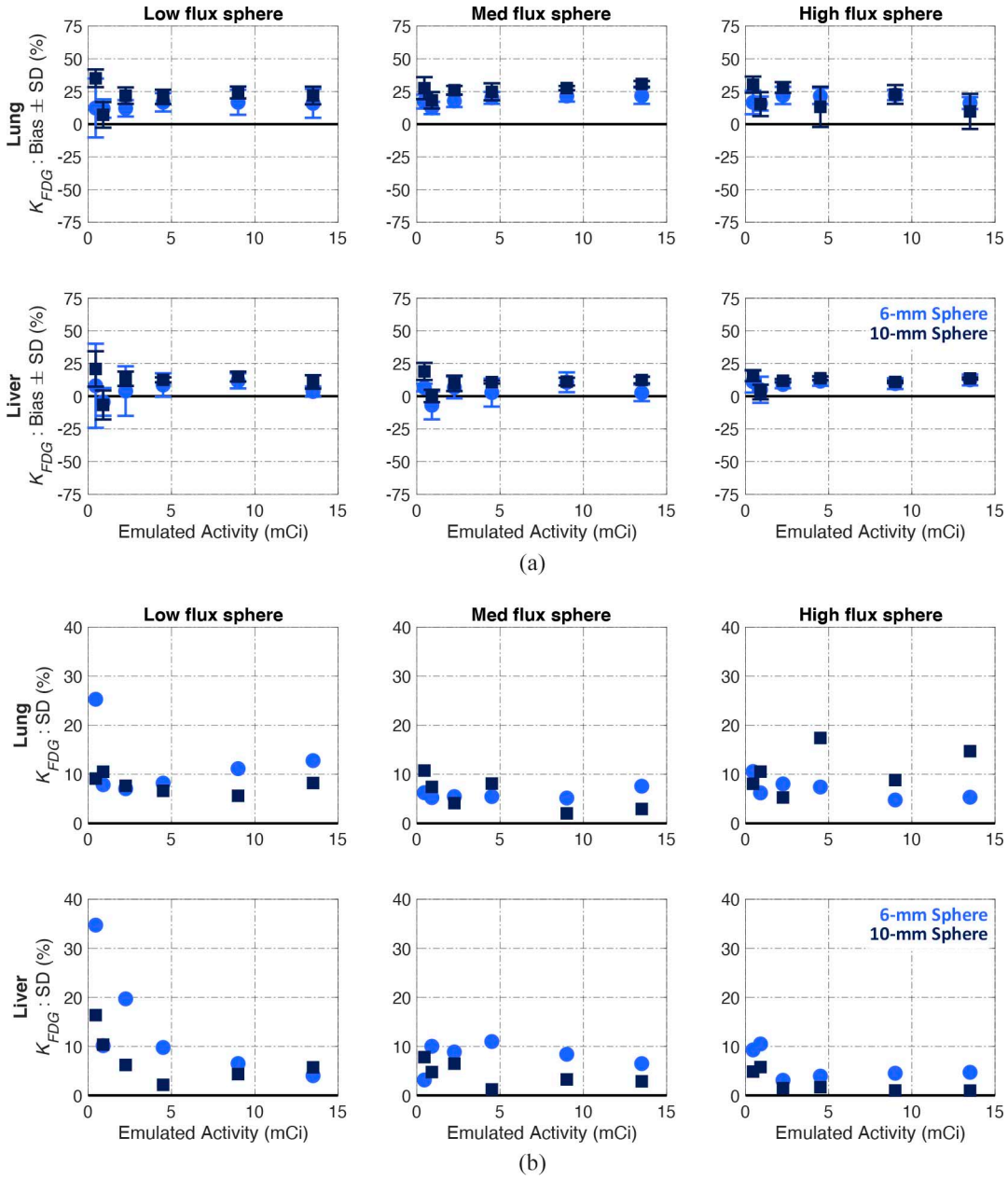

Fig. 10. (a) Bias and (b) % SD results quantifying flux (K_{FDG}) using a two-compartmental fit as measured from the FDG PennPET Explorer emulation for the 6-mm sphere (lighter blue) and the 10-mm sphere (dark blue). Results are shown for the low, medium, and high (left to right) flux spheres and for the lung (top) and liver (bottom).

flux lesions and at lower administered activities. With the 70-cm scanner, the bias of flux is near zero for medium and high flux lesions. The precision of flux estimation is better over a wide range of emulated doses for the 70-cm scanner geometry compared to the 23-cm scanner geometry, with some noticeable loss of precision for doses less than 1 mCi.

A dynamic FDG study with embedded lesions was then used to study the performance of a long AFOV scanner. Patlak graphical analysis of dynamic data (Fig. 9), show a near-zero bias and low % SD for all fluxes over a wide range of doses. The combination of the increased sensitivity afforded by the PennPET Explorer and Patlak graphical analysis allows for quantitatively accurate dynamic imaging with low administered activity which is especially desirable in certain populations, such as pediatric imaging. Because a subset of lesions and the left ventricle (the source of the blood input function) were located in the axial range of the PennPET Explorer's data readout inactive regions, a single-ring analysis of these embedded lesions was not possible. However, we estimate that a standard AFOV system would need three times the administered activity, based on gains in axial sensitivity, to achieve the same quantitative accuracy as the PennPET Explorer, underscoring the benefits of such a long AFOV scanner [21].

Patlak analysis allows for quantification of flux but cannot estimate delivery of FDG (K_1). K_1 has been shown to

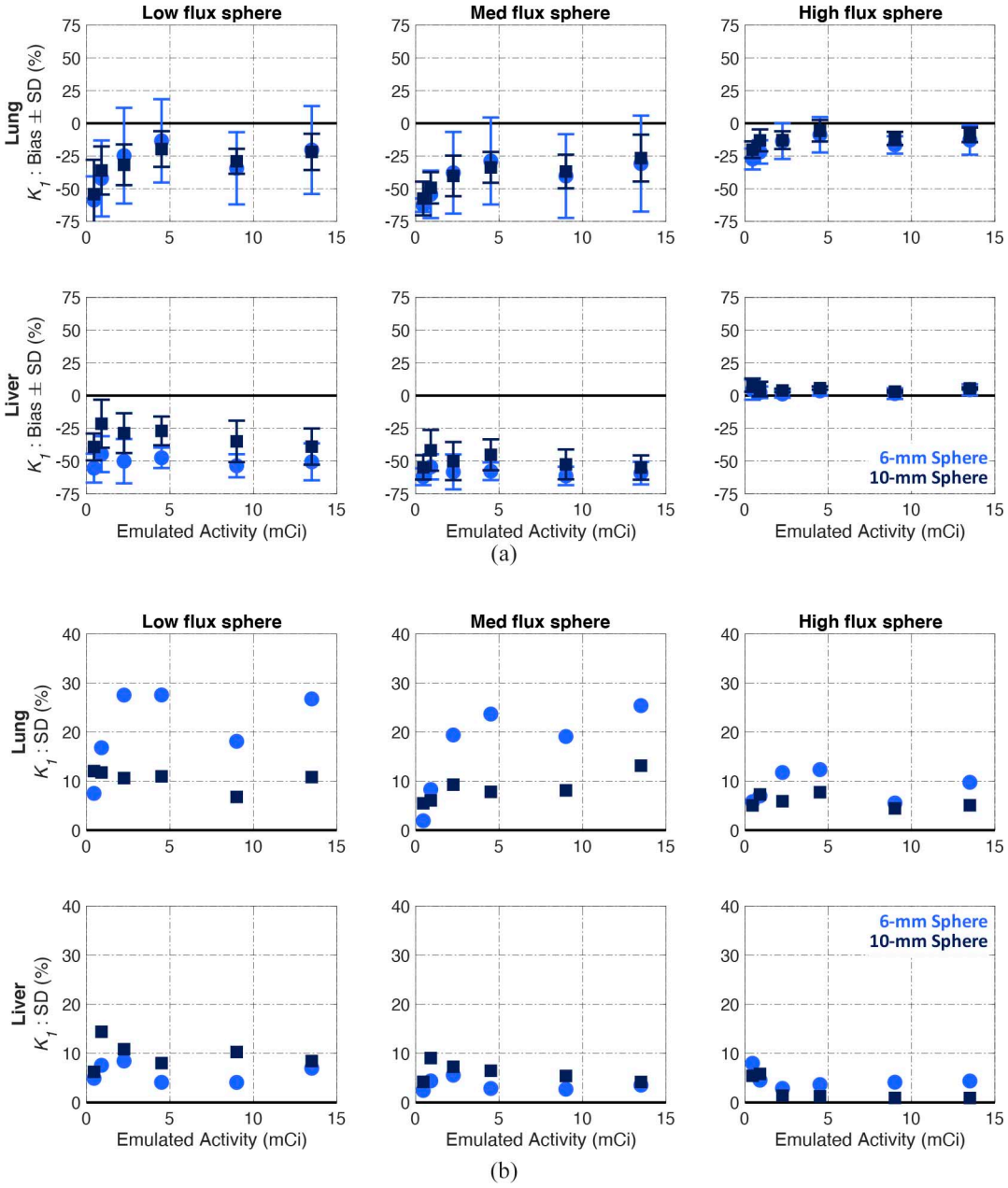

Fig. 11. (a) Bias and (b) % SD results quantifying delivery (K_1) using a two-tissue-compartmental fit as measured from the FDG PennPET Explorer emulation for the 6-mm sphere (medium blue) and the 10-mm sphere (dark blue). Results are shown for the low, medium, and high (left to right) flux spheres and for the lung (top) and liver (bottom) spheres.

have clinical prognostic value (e.g., K_1 has been shown to be predictive for breast cancer response assessment [50]). As such, we also fit the FDG data using a standard two-tissue-compartment model capable of estimating K_1 in addition to flux. Results (Fig. 10) show a systematically positive bias for all spheres that was stable over nearly the entire range of doses, but with lower % SD compared to Patlak analysis. The positive bias remained when fitting using calculated weighting (Poisson weighting of the measured value, frame duration, and decay based on the frame mid-time) or various fixed blood fraction values (not shown). These results suggest that the observed bias in estimated FDG flux was not due to poor parameter optimization. Although the bias of flux in the liver improved when the blood fraction value was floated, the corresponding bias of K_1 values increased to 50–100%. Bias results similarly show a larger dynamic dose range over which patients can be imaged on long AFOV scanners compared to standard AFOV scanners with one-third of the axial sensitivity. Additionally, flux estimates using Patlak analysis demonstrated consistently less bias than those obtained with the compartmental model underscoring the robustness of graphical methods.

The K_1 estimates from the dynamic FDG study with lesion embedding fit using a two-tissue-compartment model (Fig. 11) show a negative bias for the low and medium flux spheres but very little bias for the high flux spheres. Because fitting K_1 depends on the early portion of the TAC, these inaccuracies

may result from noise in the lesion TAC of the 1-s time frames during the first few minutes. Since uptake is higher for the high flux spheres in the early time points, these spheres were more accurately measured, resulting in less noise and more accurate quantification of K_1. This conclusion is further supported by noting that the 6-mm spheres show greater bias and greater % SD compared to the 10-mm spheres, and the K_1 estimates from the FLT simulation, which were sampled with 5-s frames, show a bias close to zero. Therefore, although 1-s time frames allow us to capture the peak of the blood input curve, longer time frames may be necessary to accurately quantify K_1 in small, low-uptake dynamic lesions.

This work extended the lesion embedding methodology that has previously been implemented in list-mode to an implementation in histo-images, which allows for embedding of spheres that have uptakes both higher and lower than background. This method is similar to the original lesion embedding method in sinogram space but preserves the TOF information of the spheres. Contrary to the GATE simulations of the modified NEMA IQ phantom, where dynamic uptake of the spheres was inherent in the simulation, the lesion embedding study relied on this modified methodology to properly embed lesions in the dataset. After applying a PVC and scanner calibration factor to the reconstructed images from the lesion embedding study, identical to the GATE simulations, results show proper recovery of the ideal TACs (Fig. 8) with some noise across the various lesions.

Lower emulated doses for both studies were based on uniformly subsampling list-mode data based on the number of counts. However, when injecting lower radiotracer doses, there are also count rate effects that we did not model by subsampling. Most notably, the number of random events detected would decrease quadratically compared to the number of true events detected, which decrease linearly for a higher true even fraction [51]. This would generally improve IQ and quantification of kinetic parameters, so the results obtained in this study are a conservative measure of the improvement obtained in actual dynamic studies.

A limited number of tracers and models were studied in this work. Although it is expected that any kinetic model or graphical analysis method would benefit from the use of a long AFOV system, the degree of improvement in accuracy and precision cannot be directly inferred from the findings of this study, as each method is characterized by a different level of robustness to noise. Additionally, there are organs, most commonly the liver, with nonzero k_4 when imaging with FDG and alternative modeling approaches may be necessary when k_4 is positive [52]. However, the TACs that were used to embed the spheres were generated using a two-tissue-compartment model with $k_4 = 0$.

The FLT study used twenty bootstrapped replicates, while the FDG study embedded 16 lesions in the lung and 10 lesions in the liver. While this was not sufficient to perform statistical analyses of significance and calculate p-values, it was sufficient to provide good estimates of bias and precision as a function of dose for a long AFOV scanner. Future studies would be needed to verify the statistical significance of our findings.

Additionally, this study does not make a comparison to whole-body dynamic imaging with a standard AFOV system, where early dynamic data are collected over the left-ventricle to capture the blood input followed by multiple sweeps of the whole body [7], [8]. The protocol proposed by Karakatsanis *et al.* includes a 6-min dynamic scan over the heart followed by 5-min whole-body sweeps where data in each bed position are acquired for 45 s. This method dynamically images the whole body, but with coarse temporal sampling of TACs. For long AFOV scanners that are less than a meter long and do not fully cover organs of interest in a single bed position (e.g., brain and pelvis), this method may prove useful to image distant organs or lesions.

Both studies were processed using a PVC that relied on known information that would not be known for an actual dynamic study. Our PVC correction was unique to this study and could not be used for dynamic human studies on the PennPET Explorer. Our method depended on knowing the true contrast to background ratio of the lesion in each frame and the lesion size. This was done for our study to avoid introducing bias in the measurement of the TACs; however, while tumor size could be estimated from a CT, the true contrast of the lesion would not be known for a real dynamic study. An alternative method that could be employed for measured dynamic data is to use the measured contrast of the sphere and the CRC for a lesion of that size to estimate the true sphere contrast. However, that method increases noise in the measured TACs and the PVC for this study was designed to avoid compounding noise from measurement.

Finally, while we reconstructed data frame-by-frame and fit data after reconstruction, there may be advantages to utilize direct parametric image reconstruction algorithms to reduce noise in the estimated kinetic parameters [26], [53]–[55]. While it is outside the scope of this work, the dynamic FDG data with embedded lesions created and studied for this work is currently being used to test a direct Patlak reconstruction method using the DIRECT framework.

V. Conclusion

The increased sensitivity of a long AFOV PET scanner improved the quantitative accuracy of kinetic parameters estimation across a range of injected activities (0.5–2 mCi), compared to standard AFOV (<30 cm) PET scanners, depending on lesion size, and dynamic uptake features. The ability to lower the dose on these scanners will reduce patient exposure for dynamic studies that are often experimental research protocols and ease production requirements for less commonly used radiopharmaceuticals for both research and clinical use. Since many research tracers are injected at around 5 mCi (185 MBq) due to organ dose limitations or radiopharmaceutical production limits, imaging these tracers on a long AFOV scanner will particularly benefit quantification of kinetic parameters for research studies. Although these studies used two ^{18}F labeled tracers, results can be generalized to other radioisotopes such as ^{68}Ga or ^{89}Zr which are gaining popularity. Finally, these results are also generalizable to AFOVs longer than 70-cm which would allow for accurate kinetic parameter estimation

of dynamic studies with multiple lesions in organs spread throughout an even larger axial extent.

ACKNOWLEDGMENT

The clinical studies were made possible by contributions from Erin Schubert, Michael Parma, and Janet Reddin, Ph.D. The authors thank their collaborators at the University of Washington for sharing FLT data that made this work possible.

REFERENCES

[1] R. K. Doot, E. S. McDonald, and D. A. Mankoff, "Role of PET quantitation in the monitoring of cancer response to treatment: Review of approaches and human clinical trials," *Clin. Transl. Imag.*, vol. 2, no. 4, pp. 295–303, 2014.

[2] R. E. Carson and P. H. Kuo, "Brain-dedicated emission tomography systems: A perspective on requirements for clinical research and clinical needs in brain imaging," *IEEE Trans. Radiat. Plasma Med. Sci.*, vol. 3, no. 3, pp. 254–261, May 2019.

[3] J.-D. Gallezot, Y. Lu, M. Naganawa, and R. E. Carson, "Parametric imaging with PET and SPECT," *IEEE Trans. Radiat. Plasma Med. Sci.*, vol. 4, no. 1, pp. 1–23, Jan. 2020.

[4] M. Muzi *et al.*, "Quantitative assessment of dynamic PET imaging data in cancer imaging," *Magn. Reson. Imag.*, vol. 30, no. 9, pp. 1203–1215, 2012.

[5] S. R. Cherry, R. D. Badawi, J. S. Karp, W. W. Moses, P. Price, and T. Jones, "Total-body imaging: Transforming the role of positron emission tomography," *Sci. Transl. Med.*, vol. 9, no. 381, 2017, Art. no. eaaf6169.

[6] S. R. Cherry, T. Jones, J. S. Karp, J. Qi, W. W. Moses, and R. D. Badawi, "Total-body PET: Maximizing sensitivity to create new opportunities for clinical research and patient care," *J. Nucl. Med.*, vol. 59, no. 1, pp. 3–12, 2018.

[7] N. A. Karakatsanis, M. A. Lodge, A. K. Tahari, Y. Zhou, R. L. Wahl, and A. Rahmim, "Dynamic whole-body PET parametric imaging: I. Concept, acquisition protocol optimization and clinical application," *Phys. Med. Biol.*, vol. 58, no. 20, pp. 7391–7418, 2013.

[8] N. A. Karakatsanis, M. A. Lodge, Y. Zhou, R. L. Wahl, and A. Rahmim, "Dynamic whole-body PET parametric imaging: II. Task-oriented statistical estimation," *Phys. Med. Biol.*, vol. 58, no. 20, pp. 7419–7445, 2013.

[9] T. Yamaya *et al.*, "A proposal of an open PET geometry," *Phys. Med. Biol.*, vol. 53, no. 3, pp. 757–773, 2008.

[10] T. Yamaya *et al.*, "Development of a small prototype for a proof-of-concept of OpenPET imaging," *Phys. Med. Biol.*, vol. 56, no. 4, pp. 1123–1137, 2011.

[11] J. Zhang, M. I. Knopp, and M. V. Knopp, "Sparse detector configuration in SiPM digital photon counting PET: A feasibility study," *Mol. Imag. Biol.*, vol. 21, no. 3, pp. 447–453, 2019.

[12] S. A. Zein, N. A. Karakatsanis, M. Issa, A. A. Haj-Ali, and S. A. Nehmeh, "Physical performance of a long axial field-of-view PET scanner prototype with sparse rings configuration: A Monte Carlo simulation study," *Med. Phys.*, vol. 47, no. 4, pp. 1949–1957, 2020.

[13] J. van Sluis *et al.*, "Performance characteristics of the digital biograph vision PET/CT system," *J. Nucl. Med.*, vol. 60, no. 7, pp. 1031–1036, 2019.

[14] I. Rausch, A. Ruiz, I. Valverde-Pascual, J. Cal-González, T. Beyer, and I. Carrio, "Performance evaluation of the Vereos PET/CT system according to the NEMA NU2-2012 standard," *J. Nucl. Med.*, vol. 60, no. 4, pp. 561–567, 2019.

[15] J. A. Kolthammer, K.-H. Su, A. Grover, M. Narayanan, D. W. Jordan, and R. F. Muzic, "Performance evaluation of the ingenuity TF PET/CT scanner with a focus on high count-rate conditions," *Phys. Med. Biol.*, vol. 59, no. 14, pp. 3843–3859, 2014.

[16] B. Jakoby, Y. Bercier, M. Conti, M. Casey, B. Bendriem, and D. Townsend, "Physical and clinical performance of the mCT time-of-flight PET/CT scanner," *Phys. Med. Biol.*, vol. 56, no. 8, pp. 2375–2389, 2011.

[17] T. Pan *et al.*, "Performance evaluation of the 5-ring GE discovery MI PET/CT system using the national electrical manufacturers association NU 2-2012 standard," *Med. Phys.*, vol. 46, no. 7, pp. 3025–3033, 2019.

[18] S. Surti, A. R. Pantel, and J. S. Karp, "Total body PET: Why, how, what for?" *IEEE Trans. Radiat. Plasma Med. Sci.*, vol. 4, no. 3, pp. 283–292, Apr. 2020.

[19] J. S. Karp *et al.*, "PennPET explorer: Design and preliminary performance of a whole-body imager," *J. Nucl. Med.*, vol. 61, no. 1, pp. 136–143, 2019.

[20] R. D. Badawi *et al.*, "First human imaging studies with the EXPLORER total-body PET scanner," *J. Nucl. Med.*, vol. 60, no. 3, pp. 299–303, 2019.

[21] V. Viswanath *et al.*, "GATE simulations to study extended axial FOVs for the PennPET explorer scanner," in *Proc. IEEE NSS/MIC*, 2017, pp. 1–5.

[22] S. Surti and J. Karp, "Impact of detector design on imaging performance of a long axial field-of-view, whole-body PET scanner," *Phys. Med. Biol.*, vol. 60, no. 13, pp. 5343–5358, 2015.

[23] S. Surti, A. R. Shore, and J. S. Karp, "Design study of a whole-body PET scanner with improved spatial and timing resolution," *IEEE Trans. Nucl. Sci.*, vol. 60, no. 5, pp. 3220–3226, Jul. 2013.

[24] V. Viswanath, M. E. D. Witherspoon, J. S. Karp, and S. Surti, "Numerical observer study of lesion detectability for a long axial field-of-view whole-body PET imager using the PennPET explorer," *Phys. Med. Biol.*, vol. 65, no. 3, 2020, Art. no. 035002.

[25] A. R. Pantel *et al.*, "PennPET explorer: Human imaging on a whole-body imager," *J. Nucl. Med.*, vol. 61, no. 1, pp. 144–151, 2019.

[26] X. Zhang *et al.*, "Total-body parametric imaging using kernel and direct reconstruction on the uEXPLORER," *J. Nucl. Med.*, vol. 60, no. S1, p. 456, 2019.

[27] G. Wang *et al.*, "Quantification of glucose transport using high temporal resolution dynamic PET imaging," *J. Nucl. Med.*, vol. 60, no. S1, p. 521, 2019.

[28] X. Zhang *et al.*, "Subsecond total-body imaging using ultrasensitive positron emission tomography," *Proc. Nat. Acad. Sci.*, vol. 117, no. 5, pp. 2265–2267, 2020.

[29] M. Muzi *et al.*, "Kinetic analysis of 3'-deoxy-3'-fluorothymidine PET studies: Validation studies in patients with lung cancer," *J. Nucl. Med.*, vol. 46, no. 2, pp. 274–282, 2005.

[30] M. Muzi, D. A. Mankoff, J. R. Grierson, J. M. Wells, H. Vesselle, and K. A. Krohn, "Kinetic modeling of 3'-deoxy-3'-fluorothymidine in somatic tumors: Mathematical studies," *J. Nucl. Med.*, vol. 46, no. 2, pp. 371–380, 2005.

[31] H. Minn, K. R. Zasadny, L. E. Quint, and R. L. Wahl, "Lung cancer: Reproducibility of quantitative measurements for evaluating 2-[F-18]-fluoro-2-deoxy-D-glucose uptake at PET," *Radiology*, vol. 196, no. 1, pp. 167–173, 1995.

[32] A. Dimitrakopoulou-Strauss *et al.*, "Prognostic aspects of 18F-FDG PET kinetics in patients with metastatic colorectal carcinoma receiving FOLFOX chemotherapy," *J. Nucl. Med.*, vol. 45, no. 9, pp. 1480–1487, 2004.

[33] A. Dimitrakopoulou-Strauss *et al.*, "Quantitative assessment of SSTR2 expression in patients with non-small cell lung cancer using 68 Ga-DOTATOC PET and comparison with 18 F-FDG PET," *Eur. J. Nucl. Med. Mol. Imag.*, vol. 33, no. 7, pp. 823–830, 2006.

[34] M. Graham, L. Peterson, and R. Hayward, "Comparison of simplified quantitative analyses of FDG uptake," *Nucl. Med. Biol.*, vol. 27, no. 7, pp. 647–655, 2000.

[35] J. Strydhorst and I. Buvat, "Redesign of the GATE PET coincidence sorter," *Phys. Med. Biol.*, vol. 61, no. 18, pp. N522–N531, 2016.

[36] P. R. A. Trindade *et al.*, "GATE simulation of the Philips Vereos digital photon counting PET system NEMA NU2–2012 characterization," in *Proc. IEEE NSS/MIC*, San Diego, CA, USA, 2015.

[37] D. L. Bailey, D. W. Townsend, P. E. Kinahan, S. Grootoonk, and T. Jones, "An investigation of factors affecting detector and geometric correction in normalization of 3-D PET data," *IEEE Trans. Nucl. Sci.*, vol. 43, no. 6, pp. 3300–3307, Dec. 1996.

[38] A. Salskov, V. S. Tammisetti, J. Grierson, and H. Vesselle, "FLT: Measuring tumor cell proliferation *in vivo* with positron emission tomography and 3'-deoxy-3'-[18F] fluorothymidine," *Seminar Nucl. Med.*, vol. 37, no. 6, pp. 429–439, 2007.

[39] *NEMA Standards Publication NU-2-2018: Performance Measurements of Positron Emission Tomography*. Rosslyn, VA, USA: Nat. Elect. Manuf. Assoc., 2018.

[40] M. Dahlbom, "Estimation of image noise in PET using the bootstrap method," *IEEE Trans. Nucl. Sci.*, vol. 49, no. 5, pp. 2062–2066, Nov. 2002.

[41] L. M. Popescu, S. Matej, and R. M. Lewitt, "Iterative image reconstruction using geometrically ordered subsets with list-mode data," in *Proc. IEEE Nucl. Sci. Symp.*, vol. 6, 2004, pp. 3536–3540.

[42] M. E. Werner, S. Surti, and J. S. Karp, "Implementation and evaluation of a 3D PET single scatter simulation with TOF modeling," in *Proc. IEEE Nucl. Sci. Symp.*, vol. 3, 2006, pp. 1768–1773.

[43] D. A. Mankoff, A. F. Shields, M. M. Graham, J. M. Link, J. F. Eary, and K. A. Krohn, "Kinetic analysis of 2-[carbon-11] thymidine PET imaging studies: Compartmental model and mathematical analysis," *J. Nucl. Med.*, vol. 39, no. 6, pp. 1043–1055, 1998.

[44] R. K. Doot, "Getting the most out of 18F-FDG PET scans: The predictive value of 18F-FDG PET-derived blood flow estimates for breast cancer," *J. Nucl. Med.*, vol. 57, no. 11, pp. 1667–1668, 2016.

[45] M. E. Daube-Witherspoon, S. Surti, A. E. Perkins, and J. S. Karp, "Determination of accuracy and precision of lesion uptake measurements in human subjects with time-of-flight PET," *J. Nucl. Med.*, vol. 55, no. 4, pp. 602–607, 2014.

[46] S. Matej, S. Surti, S. Jayanthi, M. E. Daube-Witherspoon, R. M. Lewitt, and J. S. Karp, "Efficient 3-D TOF PET reconstruction using view-grouped histo-images: DIRECT—Direct image reconstruction for TOF," *IEEE Trans. Med. Imag.*, vol. 28, no. 5, pp. 739–751, May 2009.

[47] S. Matej and J. Browne, "Performance of a fast maximum likelihood algorithm for fully 3D PET reconstruction," in *Three-Dimensional Image Reconstruction in Radiology and Nuclear Medicine*. Dordrecht, The Netherlands: Kluwer Acad. Publ., 1996, pp. 297–315.

[48] M. E. Daube-Witherspoon, S. Matej, J. Karp, and R. M. Lewitt, "Application of the row action maximum likelihood algorithm with spherical basis functions to clinical PET imaging," *IEEE Trans. Nucl. Sci.*, vol. 48, no. 1, pp. 24–30, Feb. 2001.

[49] C. S. Patlak and R. G. Blasberg, "Graphical evaluation of blood-to-brain transfer constants from multiple-time uptake data. Generalizations," *J. Cerebr. Blood Flow Metab.*, vol. 5, no. 4, pp. 584–590, 1985.

[50] L. K. Dunnwald *et al.*, "PET tumor metabolism in locally advanced breast cancer patients undergoing neoadjuvant chemotherapy: Value of static versus kinetic measures of fluorodeoxyglucose uptake," *Clin. Cancer Res.*, vol. 17, no. 8, pp. 2400–2409, 2011.

[51] V. Viswanath *et al.*, "Development of PET for total-body imaging," *Acta Phys Polonica B*, vol. 48, no. 10, pp. 1555–1566, 2017.

[52] A. Dimitrakopoulou-Strauss, L. Pan, and C. Sachpekidis, "Kinetic modeling and parametric imaging with dynamic PET for oncological applications: General considerations, current clinical applications, and future perspectives," *Eur. J. Nucl. Med. Mol. Imag.*, to be published.

[53] N. A. Karakatsanis, M. E. Casey, M. A. Lodge, A. Rahmim, and H. Zaidi, "Whole-body direct 4D parametric PET imaging employing nested generalized Patlak expectation–maximization reconstruction," *Phys. Med. Biol.*, vol. 61, no. 15, pp. 5456–5485, 2016.

[54] G. Wang, L. Fu, and J. Qi, "Maximum *a posteriori* reconstruction of the Patlak parametric image from sinograms in dynamic PET," *Phys. Med. Biol.*, vol. 53, no. 3, pp. 593–604, 2008.

[55] W. Zhu, Q. Li, B. Bai, P. S. Conti, and R. M. Leahy, "Patlak image estimation from dual time-point list-mode PET data," *IEEE Trans. Med. Imag.*, vol. 33, no. 4, pp. 913–924, Apr. 2014.